Journal of
Materials Chemistry A

ROYAL SOCIETY
OF CHEMISTRY

PAPER

View Article Online
View Journal | View Issue

Check for updates

Cite this: *J. Mater. Chem. A*, 2023, **11**, 14809

Modulating and optimizing 2D/2D Fe-$Ni_2P/ZnIn_2S_4$ with S vacancy through surface engineering for efficient photocatalytic H_2 evolution†

Guanqiong Li,[a] Haiou Liang,[a] Xiaoye Fan,[a] Xiaoling Lv,[c] Xingwei Sun, *[a] Heng-guo Wang *[b] and Jie Bai *[a]

Received 27th April 2023
Accepted 12th June 2023

DOI: 10.1039/d3ta02519e

rsc.li/materials-a

Photocatalytic hydrogen release provides a sustainable and promising method for solar energy fuels and raw materials. The reasonable construction of nanocomposite photocatalysts with rapid charge transfer and broad solar response capability is of great significance for the efficient conversion of solar energy to chemical energy. Herein, for the first time, different metal ions (Fe, Co, and Mn) are doped *in situ* through the surface modification strategy to change the electronic structure and d band center of the cocatalyst Ni_2P, which then adjusts the surface state of $ZnIn_2S_4$ nanosheets with S defects to accelerate the surface photocatalytic hydrogen evolution reaction. It is impressive that the constructed Fe-doped $Ni_2P/ZnIn_2S_4$-Vs ultra-thin 2D/2D nanosheet structure has the best photocatalytic hydrogen evolution activity and lasts for 20 h, and its hydrogen evolution rate can reach 4548.75 μmol g^{-1} h^{-1}, which is 11.51-fold higher than that of pristine $ZnIn_2S_4$. Moreover, the simulation results indicate that Fe doping replaces the Ni site and also confirm the path of charge directional transfer. The composite catalyst optimizes the Gibbs free energy of the intermediate state of the hydrogen evolution reaction, thus improving intrinsic photocatalytic activity. This study provides guidance for the construction of a highly efficient hydrogen evolution photocatalyst.

1. Introduction

The continuous production of H_2 from water using solar semiconductors to achieve the conversion of solar energy to green hydrogen energy is considered a feasible solution for solving energy and environmental problems. The development of efficient, durable, and nontoxic photocatalysts for the hydrogen evolution reaction (HER) from water remains a great challenge. Among many photocatalysts, zinc indium sulfide (ZIS) is a promising transition metal sulfide semiconductor photocatalyst.[1–6] As a typical ternary-layered structure, its band gap is tunable (2.06–2.85 eV), and the conduction band is about −1.21 eV, representing the strong reducing ability of photogenerated electrons. In addition to the appropriate band gap structure, ZIS has a friendliness and excellent photostability environment compared with commonly used CdS and PbS.[7–10] However, there are still problems, such as a narrow light absorption range, short photogenerated carrier lifetime, and severe recombination in applications, which limit its photocatalytic efficiency and practical application.[11–13] In pursuit of better photocatalytic performance, researchers have made great efforts in morphology regulation, defect engineering, element doping, and cocatalyst loading, which have achieved satisfactory modification results.[14–17]

It is well known that is an effective introduction of vacancy into ultrathin layer-structured semiconductors can improve the

Xingwei Sun is a lecturer at the School of Chemical Engineering, Inner Mongolia University of Technology. In December 2021, she received her PhD in Chemistry and Technology from the Inner Mongolia University of Technology. She published 7 papers as the first author during her PhD and presided over a fund of the autonomous region. She is engaged in basic and applied research on new energy materials and devices. At present, the main research fields are electrocatalytic water splitting, supercapacitors, and zinc-air batteries.

---

[a] *Chemical Engineering College, Inner Mongolia University of Technology, Huhhot, 010051, P. R. China. E-mail: sxw@imut.edu.cn; baijie@imut.edu.cn*

[b] *Key Laboratory of Polyoxometalate and Reticular Material Chemistry of Ministry of Education and Faculty of Chemistry, Northeast Normal University, Changchun 130022, P. R. China. E-mail: wanghg061@nenu.edu.cn*

[c] *School of Materials Science and Engineering, Changchun University of Science and Technology, Changchun 130022, P. R. China*

† Electronic supplementary information (ESI) available. See DOI: **https://doi.org/10.1039/d3ta02519e**

electronic structure of catalysts. The effect of vacancy can lead to the emergence of the intermediate energy level to narrow the intrinsic band gap of the semiconductor photocatalysts and can effectively adjust the charge transfer kinetics to capture photogenerated electrons, thus modulating the electron spatial distribution and prolonging the lifetime.[18,19] Importantly, the controllable adjustment of the vacancy concentration has a direct relationship to photocatalytic performance, but the excess vacancies can become recombination centers for photogenerated carriers, thereby suppressing photocatalytic performance. In this context, vacancy-rich semiconductor materials with good electron transfer properties have attracted considerable attention from researchers.[20] Hence, adjusting the vacancy to the appropriate concentration is beneficial for optimizing the property and stability of the photocatalyst. However, based on the reported literature, only introducing defects is insufficient to achieve efficient photocatalytic performance.[21]

In recent years, as typical representatives of emerging non-precious photocatalysts, transition metal phosphides (TMPs), such as Ni_2P, Co_2P, and MoP, have been considered substitutes for noble metals owing to their excellent electrical conductivity. It is inexpensive, non-toxic, good in hydrophilicity, and suitable hydrogen adsorption free energy and exhibits noble metal-like properties for HER. In this regard, Ni_2P as a cocatalyst is very excellent and has received extensive attention. Recent literature has confirmed that the assembly of Ni_2P nanoparticles with semiconductors can achieve high photocatalytic hydrogen production efficiency. Compared with nanoparticles, two-dimensional (2D) Ni_2P has been widely used as an ideal material because of its larger specific surface area, shorter carrier migration distance and richer active sites. Some studies have found that when the 2D-layered structure is reduced to ultra-thin size, it will have unexpected effects.[22–25] Therefore, it is a good choice to introduce 2D Ni_2P into metal sulfide.[26] However, as far as we know, there are still some limitations in their combination and photocatalytic performance. For example, although the two semiconductors are in close contact, interface bonding is not considered.

Based on the above considerations, if the vacancies are constructed on ZIS, which is then modified *via* 2D Ni_2P, the two phases form a tight bonding effect through the vacancies, thus giving full play to the synergistic effects resulting from their respective advantages. Therefore, we intelligently design and synthesize 2D/2D Fe-doped Ni_2P modified ZIS with rich S vacancies (Fe-Ni_2P/ZIS-Vs) photocatalyst for the first time *via* a solvothermal self-assembly strategy, which can improve the photocatalytic hydrogen evolution property. Herein, shortening the solvothermal time is a prerequisite for obtaining S vacancies, where S vacancies can broaden the light absorption range, and abundant unsaturated S atoms as target sites of P atoms are helpful for the *in situ* growth of Fe-doped Ni_2P on the surface of ZIS-Vs. In particular, Ni_2P acted as the active site for hydrogen evolution and was enriched with photogenerated electrons. After *in situ* doping Fe^{3+}, the local coordination environment and center position of the d-band are further adjusted, thereby reducing the kinetic energy barrier of the hydrogen evolution reaction. In addition, the tight interface bonding between Fe-Ni_2P and ZIS benefits charge transfer. As anticipated, the optimized Fe-Ni_2P/ZIS-Vs photocatalyst exhibited superior hydrogen release capacity and long-term stability, as confirmed by the characterization and DFT calculations. This study provides a new idea for maximizing transition metal phosphides as cocatalysts in the future.

2. Results and discussion

2.1 Characterizations of morphology and structure

To explore the optimal substitution position of Fe dopants in Ni_2P/ZIS-Vs composites, we performed a detailed study using theoretical calculations. The structural models of all materials are presented in Fig. S1.† As depicted in Fig. 1a–c, various 3D structural models of Fe-Ni_2P-ZIS-Vs are established, including the coordination structures of Fe doping substitution at diverse positions (Zn, In and Ni). In addition, Table S1† lists the energy changes in each active site for the alternative models. According to the calculations, the optimal substitution site for the Fe-Ni_2P-ZIS-Vs is the Ni atom, whose formation energy is the lowest. Therefore, for composites, it is highly likely that Fe will replace the Ni atom in Ni_2P and dope into the Ni_2P lattice. As summarized in Fig. 1d, the Fe-Ni_2P/ZIS-Vs material was obtained by applying a continuous solvothermal process, including the preparation of ultra-thin ZIS-Vs and the *in situ* growth of Fe-doped Ni_2P on ZIS-Vs nanosheets. By reducing the solvothermal time, ZIS nanosheets with rich S vacancies were synthesized and used as substrate materials. Subsequently, the ZIS-Vs nanosheets were immersed in the ethylenediamine solution of Ni^{2+}, Fe^{3+} and red P, and Fe-doped Ni_2P nanosheets were grown *in situ* by applying the second solvothermal process. Finally, Fe-doped Ni_2P is closely combined with ZIS-Vs nanosheets. For comparison, pure ZIS, ZIS-Vs, Ni_2P and Fe-doped Ni_2P were also synthesized.

The microscopic morphology of the as-prepared pristine ZIS powder, ZIS-Vs, Ni_2P and Fe-Ni_2P/ZIS-Vs (optimal sample) was characterized by SEM, TEM and HRTEM. As shown in Fig. 2a, the micromorphology of ZIS-Vs flower spheres comprises numerous crossed nanoflakes, similar to pristine ZIS (Fig. S2a†), which is favorable for increasing exposure to the active site. Based on the TEM image (Fig. 2b), the intersecting nanosheets are ultrathin two-dimensional structures. Moreover, in Fig. 2c (HRTEM image), a clear lattice stripe with a lattice spacing of $d = 0.32$ nm corresponds to the (102) plane of the $ZnIn_2S_4$ phase.[27] Further, obvious lattice misalignment can be surveyed in each of the shaded regions in the circle, illustrating that defect structures may be obtained by reducing the solvothermal time. From the element mapping and EDS spectrum of ZIS-Vs (Fig. S2b and c†), it could be observed that Zn, In and S elements are evenly distributed, and the atomic ratio is 1.00 : 2.00 : 3.73 (Table S2†). This represents an apparent shortage of S atoms, further demonstrating the existence of abundant S vacancies. Similarly, pure Ni_2P also comprises stacked nanosheets (Fig. S3a and b†). The HRTEM image presents one lattice spacing of 0.22 nm, which is matched to the (111) crystal planes of Ni_2P.[28] Fig. 2d and e shows SEM and TEM images of Fe-Ni_2P/ZIS-Vs, which still inherits the original

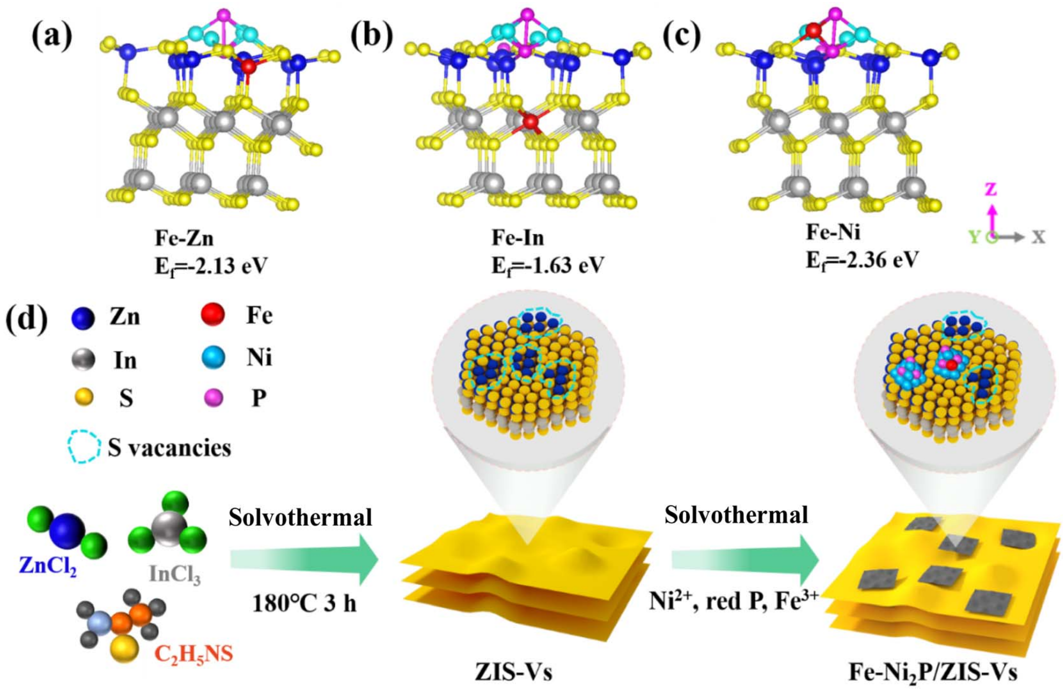

Fig. 1 Structural models for atomic Fe substituting different atoms in Fe-Ni_2P/ZIS-Vs: (a) Zn atom, (b) In atom and (c) Ni atom and corresponding formation energy (E_f). (d) Schematic illustration of the synthesis procedure of Fe-Ni_2P/ZIS-Vs.

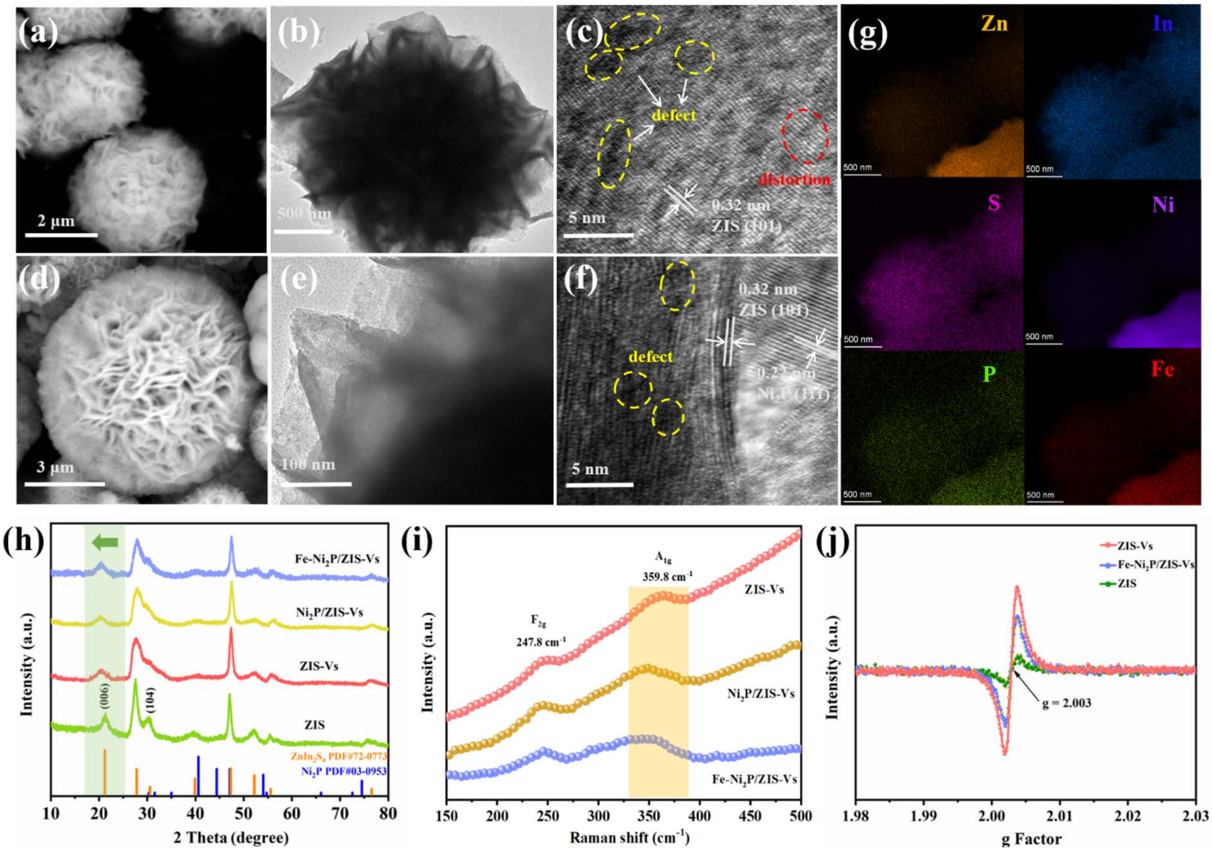

Fig. 2 (a)–(c) SEM, TEM and HRTEM images of ZIS-Vs. (d)–(f) SEM, TEM and HRTEM images of Fe-Ni_2P/ZIS-Vs. (g) Elements mapping of Zn, In, S, Fe, Ni and P of Fe-Ni_2P/ZIS-Vs. (h) XRD patterns of the ZIS, ZIS-Vs, Ni_2P/ZIS-Vs and Fe-Ni_2P/ZIS-Vs. (i) Raman spectra and (j) EPR spectra of ZIS, ZIS-Vs and Fe-Ni_2P/ZIS-Vs.

nanoflower morphology after phosphorylation treatment, which is similar to Ni_2P/ZIS-Vs (Fig. S3c†). Moreover, ZIS-Vs and Ni_2P nanosheets are difficult to distinguish, indicating that the two phases are in close contact (Fig. 2e). The multi-layer flower microsphere structure improves light absorption *via* multi-layer reflection and scattering, while the two phases in close contact facilitate rapid charge transfer, thus enhancing photocatalytic capacity. In addition, the HRTEM image displayed in Fig. 2f marks two lattice striations of widths with different *d* values of 0.22 and 0.32 nm, indicating the (102) plane of the ZIS and (111) plane of Ni_2P, respectively. The above results reveal that Ni_2P is grown directly and adheres to ZIS nano-flakes. To confirm the distribution of Fe-Ni_2P/ZIS-Vs more intuitively, the elemental mapping images are depicted in Fig. 2g. The results show that Zn, In and S elements are uniformly and densely distributed in the composites. The Ni, Fe, and P elements are relatively sparse. This indicates that the Fe-Ni_2P/ZIS-Vs has been successfully prepared. Based on the EDS spectrum (Fig. S3d†), the atomic ratio of Zn, In and S is 1.00 : 2.00 : 3.85 in the composite Fe-Ni_2P/ZIS-Vs, suggesting many S vacancies in the material (Table S3†). Simultaneously, we also determined the final content of Fe in the composite using ICP-OES. As confirmed, the content of doped Fe in Fe-Ni_2P/ZIS-Vs is around 0.6 wt%. To confirm the crystal structures of a series of prepared samples, XRD patterns were carried out (Fig. 2h). For ZIS-Vs, the main diffraction peaks agree with those of hexagonal ZIS (JCPDS No. 72-0773), which can explain the formation of high-crystalline ZIS. Interestingly, the diffraction peak of ZIS-Vs is weakened relative to ZIS, and the disappearance of the (104) plane indicates the appearance of an S vacancy.[29] Simultaneously, all the diffraction peaks of pure Ni_2P obtained by the solvent heat agreed with Ni_2P (JCPDS:03-0953) (Fig. S4†).[30] After loading Ni_2P on the ZIS-Vs substrate, the crystallinity of the composite material weakened. The diffraction peak at the (006) lattice plane obviously shifts to low angles, indicating structural distortion caused by the combination of the two phases. Owing to the low loading of Ni_2P and good dispersion, no XRD peaks corresponding to Ni_2P are observed. However, when the Ni_2P load reaches 15%, a weak diffraction peak appears, located at 44.8°, further demonstrating the successful formation of the Ni_2P/ZIS-Vs (Fig. S5†). After modification with Fe^{3+}, the diffraction peaks are essentially identical to Ni_2P/ZIS-Vs, and no separated or other phases appear. This shows that the crystal structure of Ni_2P/ZIS-Vs is insignificantly altered after the introduction of the heteroatom. Moreover, with a change amounting to Fe dopant, the peak pattern of the composite hardly changes significantly (Fig. S6†). In addition, the structural composition of the photocatalyst was further analysed by Raman spectroscopy (as depicted in Fig. 2i). As observed in the ZIS-Vs, the characteristic peaks located at 247.8 and 359.8 cm^{-1} corresponded to the F_{2g} and A_{1g} patterns of the ZIS, respectively. Compared with Ni_2P/ZIS-Vs and Fe-Ni_2P/ZIS-Vs, the F_{2g} pattern does not significantly change, and the A_{1g} pattern characteristic peak of ZIS-Vs appears evidently blue shift, which further demonstrates a strong coupling relationship between ZIS-Vs and Fe-Ni_2P.[31,32] Based on the HRTEM images of Fig. 2c and f, we found that there are many atomic vacancies in the complex. Electron paramagnetic resonance (EPR) spectroscopy was employed to further determine the type of vacancy. As shown in Fig. 2j, a weak EPR signal is detected in the ZIS, which is due to inevitable defects during sample preparation. The remaining samples all show strong EPR response signals at $g = 2.003$, revealing that successfully reducing the solvothermal time can generate many S vacancies.[33] It is well known that the intensity of the EPR signal is proportional to the electron capture centre concentration. Notably, ZIS-Vs exhibits the strongest EPR response. After loaded Fe doping Ni_2P, the EPR response intensity is greatly attenuated lower than that of ZIS-Vs. Because the structural properties of S and P are similar, this result fully proves that P from Ni_2P is selectively anchored to the vacancy structure of ZIS-Vs, resulting in a decrease in the Vs concentration in the composite.[34] According to the literature, an appropriate amount of vacancy structures can act as electron traps to enrich electrons, prolong the carrier lifetime and improve the photocatalytic hydrogen evolution capacity.[20]

2.2 Chemical composition and chemical states

The chemical states and surface composition of the catalysts were studied using X-ray photoelectron spectroscopy (XPS). XPS survey spectra show that Fe-Ni_2P/ZIS-Vs composites contain weak elements of Ni and P except for Zn, In and S (Fig. S7a†). However, the peak of Fe is unobserved, which may be due to its low content. For the high-resolution Zn 2p spectra of ZIS-Vs and Fe-Ni_2P/ZIS-Vs (Fig. S7b†), the peaks located at 1021.0 and 1044.0 eV are attributed to the Zn $2p_{3/2}$ and Zn $2p_{1/2}$ peaks of ZIS-Vs, respectively.[35,36] For In 3d spectra of ZIS-Vs (Fig. S7c†), it shows two peaks at 444.0 (In $3d_{5/2}$) and 451.5 eV (In $3d_{3/2}$), which indicate the characteristics of In^{3+}.[37] There is a slight positive shift compared with Fe-Ni_2P/ZIS-Vs. According to the literature, the S 2p binding energies of the original ZIS are 161.7 eV and 162.9 eV, respectively. The S 2p peaks of ZIS-Vs emerge a significant negative shift, which further confirms the existence of S vacancies, as illustrated in Fig. S7d.†[38] Because the S vacancy belongs to a strong electron attracting group, it can promote electron transfer, thus reducing the electron cloud density of the S atom in ZIS, resulting in lower binding energy. It is noteworthy that the binding energies of the In and S elements in Fe-Ni_2P/ZIS-Vs composites are slightly higher than those in ZIS-Vs, suggesting strong chemical bonding between the two phases.[30] As shown in Fig. S7e,† the Fe 2p spectrum of Fe-Ni_2P/ZIS-Vs can be deconvoluted into four peaks. The peaks at 711.0 and 724.4 eV are attributed to Fe(III) $2p_{3/2}$ and Fe(III) $2p_{1/2}$, respectively, and the other two peaks correspond to satellite peaks, indicating that Fe^{3+} has been successfully doped into Ni_2P.[39,40] For the high-resolution XPS spectra of the Ni element (Fig. S8a and b†), six similar peaks are found. In this case, the two peaks of binding energies at 852.0 and 869.4 eV are determined to be $Ni^{\delta+}$ (δ close to 0) from Ni_2P. The other two groups of peaks are situated at 855.2 and 873.4 eV as well as 861.0 and 879.1 eV, which are indexed to Ni $2p_{3/2}$ and Ni $2p_{1/2}$ of Ni^{2+} and the satellite peaks, respectively. Similarly, the peak at 129.2 eV belongs to $P^{\delta-}$. Because it is slightly below P ° (130.0 eV), this indicates that most of the P exists in the form of metal phosphide. The other peak centers at 132.5 eV are assigned to PO_4^{3-} environment because Ni_2P is easily oxidized.[41–44] Interestingly, it is observed that the binding energy of Ni 2p positively shifts in the XPS spectrum of Fe-Ni_2P because the electronegativity of Fe^{3+} is higher than that of Ni^{2+}. Therefore, it is more attractive to electrons, leading to the migration of electrons to Fe^{3+}. Similarly, the charge of P 2p is redistributed after Fe doping. In addition, the Ni 2p and P 2p spectra of Fe-Ni_2P/ZIS-Vs obtain electrons and move in the negative direction compared with Fe-Ni_2P (Fig. S8c and d†). These XPS results suggest that Fe doping causes charge rearrangement of the hydrogen evolution site (Ni_2P) and accelerate HER.

Based on XPS data, it is found that the introduction of Fe^{3+} causes electronic structure changes in metal ions. Therefore, the energy band structure shift of the metal in the catalyst is further investigated by ultraviolet photoelectron spectroscopy (UPS) after metal substitution (Fig. S9†). The UPS results imply that Fe doping optimizes the position of the d-band center of the material, and the d-band center of Fe-Ni_2P/ZIS-Vs moves 0.14 eV relative to Ni_2P/ZIS-Vs, which further indicates that the introduction of Fe produces an electronic effect in the catalyst and adjusts the electronic structure of the metal.

2.3 Highly enhanced photocatalytic H_2 generation activity

The hydrogen production activity of the photocatalysts was carried out under visible light using triethanolamine (TEOA) as a hole sacrificial agent without any other noble metals. As displayed in Fig. 3a and b, Ni_2P shows no catalytic performance and pristine ZIS also exhibits a low H_2 release rate because of the fast recombination of photo-generated carriers. The amount of H_2 released from vacancy-rich samples varies with the change in solvothermal time. To reveal the influence of the S vacancy on photocatalytic HER, several control tests are presented in Fig. S10a.† Among them, the ZIS-Vs obtain the highest hydrogen evolution activity by reducing the solvothermal time to 4 h. The hydrogen evolution rate of ZIS-Vs (1260.24 μmol g^{-1} h^{-1}) is 3.20 times as high as that of ZIS powder (395.03 μmol g^{-1} h^{-1}) because the S vacancies on the ZIS surface act as electron traps that can effectively suppress photo-generated electrons and hole recombination. After anchoring Ni_2P on the matrix of ZIS-Vs, the photocatalytic H_2 evolution capacity of Ni_2P/ZIS-Vs presents a volcanic curve according to the changing load of Ni_2P. Considering that Ni_2P has a noble metal-like electron transfer rate, it acts as a co-catalyst (hydrogen evolution site) to significantly enhance the hydrogen evolution rate of Ni_2P/ZIS composites. The optimal hydrogen production rate of the Ni_2P/ZIS-Vs composite is 2251.93 μmol g^{-1} h^{-1}, which is 1.79 times that of ZIS-Vs (Fig. S10b†). Further increasing the loading amount of Ni_2P, the hydrogen capacity of the sample began to decrease. This may be due to the active site coverage of ZIS caused by excess Ni_2P. This result demonstrates that the tight 2D/2D interface between ZIS-Vs and Ni_2P can accelerate the migration of interface charges; therefore, more photo-generated electrons can participate in the reaction. Subsequently, the introduction of Fe^{3+} into the synthesis process of Ni_2P can further improve its photocatalytic hydrogen evolution performance, and the maximum hydrogen production capacity can reach 4548.75 μmol g^{-1} h^{-1} with an apparent quantum yield (AQY) of 29.28% at 420 nm monochromatic light. Ni_2P is the site of hydrogen evolution after the doping of Fe^{3+}, and its d-band center shifts downward, leading to the reduction of H_2 adsorption energy. In addition, the effect of Fe doping on electrocatalytic HER performance is investigated using a standard three-electrode system at room temperature, and the results show that metal doping has a positive effect. Compared with pure Ni_2P, Fe-Ni_2P exhibits better electrocatalytic HER activity, with a smaller overpotential and Tafel slope (Fig. S11†),

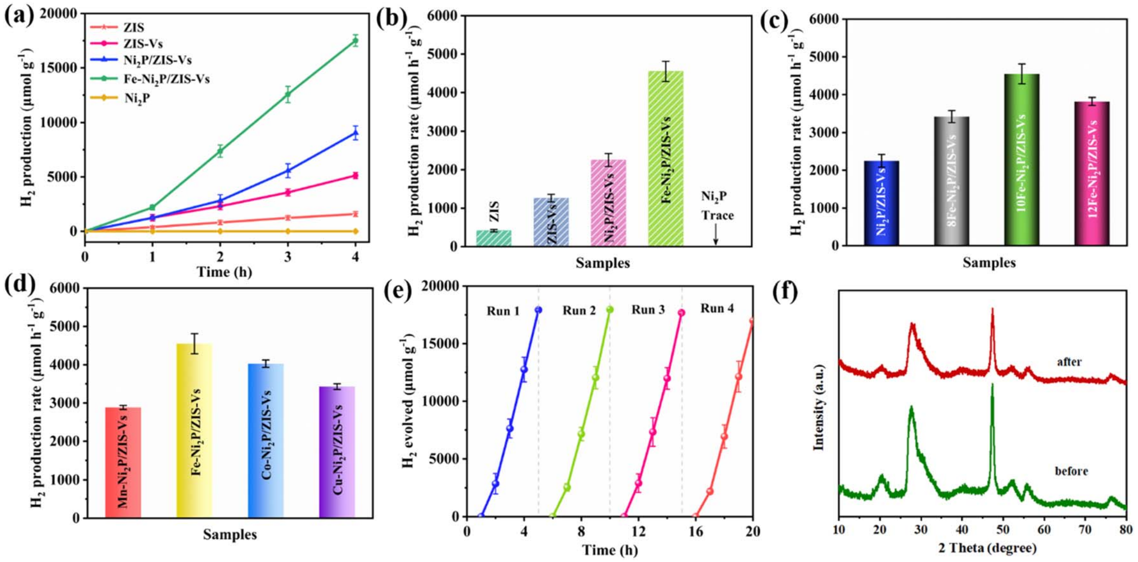

Fig. 3 (a) Time course of H_2 production. (b)–(d) The corresponding photocatalytic H_2 evolution rates of various samples. (e) The H_2 releasing yields of four successive cycles and (f) the XRD pattern of the fresh and recycled Fe-Ni_2P/ZIS-Vs samples.

indicating faster charge transfer kinetics. This acceleration capability could be owing to the modulation of the electronic structure and d-band center after metal doping. In this study, TEOA serves as an effective hole depleting agent that can promote HER. However, we must point out that the selection of sacrificial agents directly affects overall photocatalytic performance. In particular, when lactic acid (LA) and Na_2S/Na_2SO_3 are chosen as sacrificial agents, the hydrogen production performances of Fe-Ni_2P/ZIS-Vs are 2131.00 and 1335.04 μmol g^{-1} h^{-1}, respectively, which are significantly lower than those used in this study. Therefore, TEOA is a more suitable sacrificial agent in this experiment (Fig. S12†). Moreover, the hydrophilicity of the materials gradually improved (Fig. S13†). In addition, we compare the performance of the recently reported ZIS-based photocatalysts (Table S6†). Finally, we investigate the effect of introducing different metal dopants on the hydrogen production rate of Ni_2P/ZIS-Vs composite. The results indicate that metal doping has a positive effect, and Fe-Ni_2P/ZIS-Vs exhibits the best HER activity than Mn-Ni_2P/ZIS-Vs, Co-Ni_2P/ZIS-Vs and Cu-Ni_2P/ZIS-Vs (Fig. 3d). HER performance is accelerated owing to the vacancy structure and the modulation of the electronic structure after metal doping. Similarly, the cycle stability of the catalyst is also an important indicator for measuring the advantages and disadvantages of the photocatalyst. Long-cycle photocatalytic hydrogen experiments are performed to evaluate the hydrogen evolution stability of the Fe-Ni_2P/ZIS-Vs, as depicted in Fig. 3e. With the prolongation of illumination time, the cumulative amount of hydrogen gradually increases. It is noteworthy that the photocatalytic hydrogen evolution activity of Fe-Ni_2P/ZIS-Vs remains stable after 20 h of testing. As illustrated in Fig. 3f, the crystal structure of the Ni_2P/ZIS-Vs composite before and after 20 h of recycling was characterized by XRD, and the results illustrate that the characteristic peaks did not change significantly. In addition, the SEM image of Fe-Ni_2P/ZIS-Vs is still a nanoflower with an ultra-thin nanosheet structure (Fig. S14a†). Further, according to the HRTEM image and element mapping, the interface of ZIS-Vs and Fe-Ni_2P can still be found (Fig. S14b and c†), revealing that the phase interface also has high stability. In summary, the morphology and crystal phase structure of Fe-Ni_2P/ZIS-Vs are almost unchanged after the reaction, indicating that the composite has strong stability, which may be attributed to the strong combination of ZIS and Fe-Ni_2P through Vs, thereby improving the cycle stability of the composite.

2.4 Photoelectrochemical properties and energy level structure

The light-harvesting and responsiveness of the catalysts were characterized by applying ultraviolet-visible diffuse reflectance spectroscopy (UV-vis DRS) (Fig. 4a). The absorption edge of the pristine ZIS is about 500 nm, which proves that it has good light absorption and utilization capability for part of the visible light. In particular, the intrinsic absorption edge of the ZIS-Vs sample displays a red shift to 540 nm after the introduction of S vacancies. Pure Ni_2P powder is black, and when light irradiates on the surface of the sample, it absorbs the full wavelength of light and hardly reflects. Thus, owing to the full-spectrum absorption of Ni_2P, the Ni_2P-modified ZIS-Vs further exhibits a red shift in the absorption edge. From a macroscopic view, the color of Ni_2P/ZIS-Vs material gradually deepens from yellow to dark green. When Fe^{3+} is introduced and bounded into the lattice, the structure of the material's electrons is further adjusted. The light absorption edges of the Fe-doped sample are further moved to the right. Moreover, the color of the Fe-Ni_2P/ZIS-Vs sample changes from green to brown. In addition, the forbidden bandwidth of each material is calculated by employing the Kubelka–Munk function (Fig. 4b). It is evident that the construction of the vacancy and cocatalyst narrows the band gap of pristine ZIS.[45,46] It is well known that the flat band potential (E_{fb}) of the semiconductor approaches the Fermi level. By elongating the linear section of the M–S plot (Fig. 4c), it gains the E_{fb} of ZIS-Vs (−1.07 V *vs.* Ag/AgCl), which is noted over frequencies of 500 and 1000 Hz in the dark, that is −0.87 V at normal hydrogen electrodes (NHE), $E_{NHE} = E_{Ag/AgCl} + 0.197$ V. The M–S diagram slopes of the whole samples are positive, demonstrating that the material possesses an n-type semiconductor feature. The conduction band potential (E_{CB}) of the n-type semiconductor is about 0.2 V less than that of E_{fb}. Therefore, the E_{CB} of ZIS-Vs is −1.07 V (*vs.* NHE).[47,48] Based on the formula, the E_{VB} of ZIS-Vs (E_{VB} is the valence band potential) is calculated as 1.17 V (*vs.* NHE), as demonstrated in Table S4.† Finally, the band gap structure is presented in Fig. 4d. To explore the separation and transfer efficiency of photogenerated carriers of Fe-Ni_2P/ZIS-Vs, a series of optoelectronic performance measurements were performed: steady-state photoluminescence (PL) spectroscopy, time-resolved PL (TRPL) spectroscopy, transient photocurrent responses (PC), electrochemical impedance spectra (EIS) and surface photovoltage spectra (SPV). Under light excitation at 385 nm, the pristine ZIS shows the highest PL intensity, which is indicative of their high electron–hole pair recombination (Fig. 4e). The ZIS-Vs and Ni_2P/ZIS-Vs composites display obvious PL quenching phenomena. The PL strength of the composite continues to decrease when the Fe atoms are further doped.[49,50] Furthermore, the TRPL decay curves of the materials (Fig. 4f) were obtained by function fitting. As listed in Table S5,† the average lifetime of ZIS-Vs is longer than that of ZIS, indicating that proper S vacancies acting as electron traps to trap electrons can reduce the recombination of photogenerated carriers for the host. Notably, Fe-Ni_2P/ZIS-Vs has the longest average lifetime ($t_{Av} = 7.63$ ns), which is due to the fast transfer of photogenerated charges on ZIS-Vs through the two-phase interface and effectively decreases reorganization. The above results confirm that the combination of ZIS-Vs and Fe-Ni_2P is very beneficial for the separation of photogenerated carriers, which is consistent with the improvement in photocatalytic performance.[51] Fig. 4g and h correspond to the (PC) response and EIS Nyquist plot of the synthesized samples, respectively. Typically, the PC is used to characterize the charge transfer feature. All materials exhibit uniform, fast and stable photocurrent responses under intermittently cycled illumination conditions. Compared with the other samples, the composite Fe-Ni_2P/ZIS-Vs show the highest PC intensities. In general, a higher photo-generated current indicates more

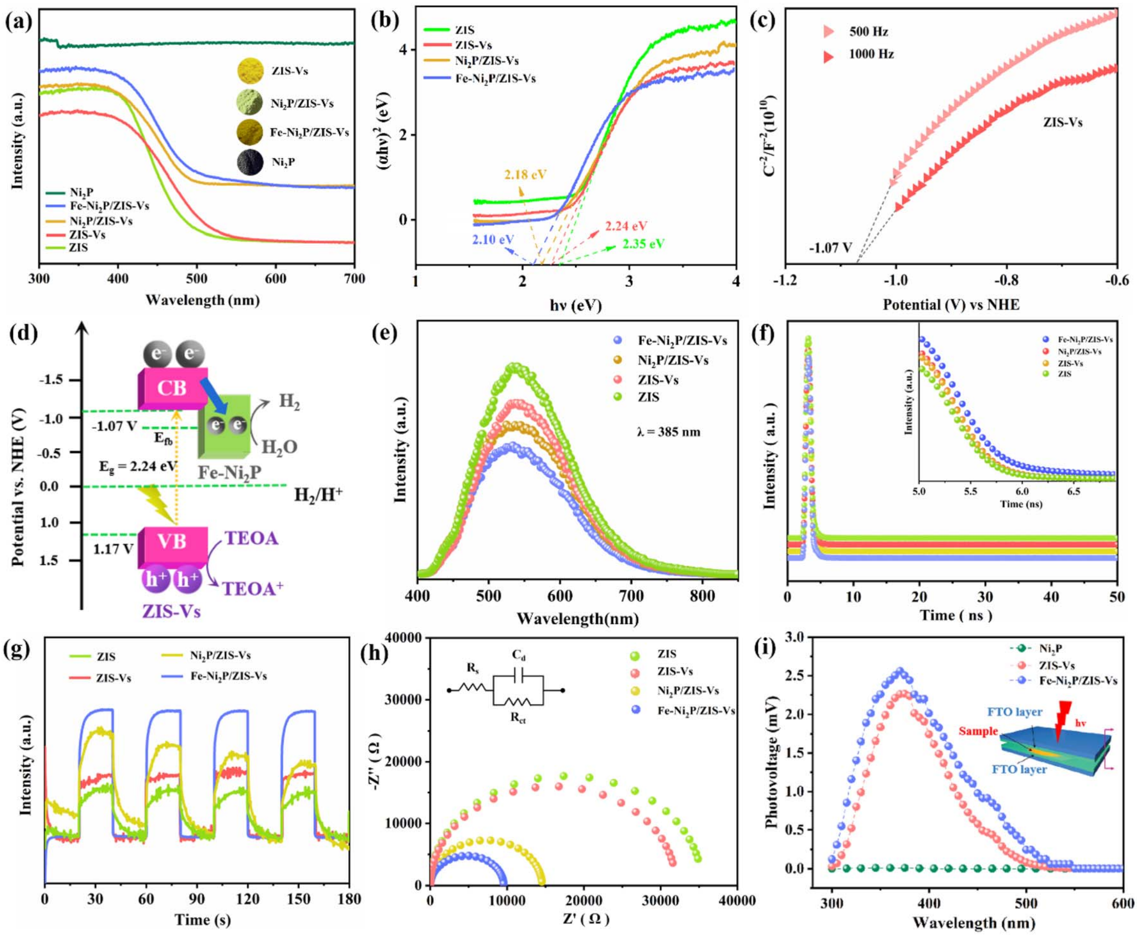

Fig. 4 (a) UV-vis absorption spectra and (b) Kubelka–Munk function *vs.* the energy of incident light plots of the as-prepared samples. (c) Mott–Schottky plots of ZIS-Vs. (d) Band structure of Fe-Ni$_2$P/ZIS-Vs sample. (e) Steady-state PL spectra, (f) TRPL decay spectra, (g) the transient PC, and (h) EIS Nyquist plots of ZIS, ZIS-Vs, Ni$_2$P/ZIS-Vs and Fe-Ni$_2$P/ZIS-Vs. (i) SPV spectra of Ni$_2$P, ZIS-Vs and Fe-Ni$_2$P/ZIS-Vs samples.

efficient separation of photo-generated carriers (Fig. 4g).[52,53] Furthermore, based on the EIS plot shown in Fig. 4h, Fe-Ni$_2$P/ZIS-Vs has the smallest arc radius. This indicates that the S deficiency and the combination with Fe-Ni$_2$P reduce the charge migration resistance in both phases. It is noteworthy that Fe-Ni$_2$P has excellent electrical conductivity, thus improving charge transfer efficiency using a contact interface. In summary, it has been proven that the composite Fe-Ni$_2$P/ZIS-Vs are the most effective for the separation and transfer of photogenerated carriers, which is conducive to HER.[54] SPV measurements were performed to explore the photoelectric effect of each sample, as demonstrated in Fig. 4i. Among them, ZIS-Vs and Fe-Ni$_2$P/ZIS-Vs have obvious positive responses in the range of 300–530 nm, indicating that the above two materials are n-type semiconductors. However, outside this range, the photovoltage value is almost zero, which corresponds to the result of UV-vis. The SPV spectrum of Ni$_2$P exhibits almost no signal, which indicates the low photo-generated charge carrier separation efficiency of the semiconductor. Thus, the huge gap between Ni$_2$P and Fe-Ni$_2$P/ZIS-Vs is attributed to the interaction at the two-phase interface. The modified Fe-Ni$_2$P/ZIS-Vs SPV response is enhanced compared to ZIS, illustrating that the photogenerated carriers are easier to separate and transfer to the surface.[18,55]

2.5 DFT calculations and photocatalytic mechanism

Density functional theory (DFT) is used to further reveal the orbital hybridization information and electron transfer trend of the two-phase contact interface. Fig. 5a depicts the charge density difference diagram of Fe-Ni$_2$P/ZIS-Vs material, where the green and yellow areas represent the electron gain and loss areas, respectively. The surface of ZIS-Vs is mainly filled by the yellow region, while the side of Fe-Ni$_2$P is a dominantly green region, which suggests that the composite has strong electron enrichment ability on the Fe-Ni$_2$P side. Furthermore, the longitudinal section image can more intuitively show the migration trend of electrons from ZIS-Vs to Fe-Ni$_2$P along the contact interface (Fig. 5b). The above analysis agrees with the XPS results.[56,57] Additionally, the Gibbs free energy (ΔG_{H^*}) of the middle state in HER represents the adsorption/desorption capacity of H*, which is a key indicator related to HER performance. As demonstrated in Fig. 5c, the calculation results indicate that Fe-Ni$_2$P/ZIS-Vs offers the lowest $\Delta G_{\mathrm{H}^*} = -0.10$ eV

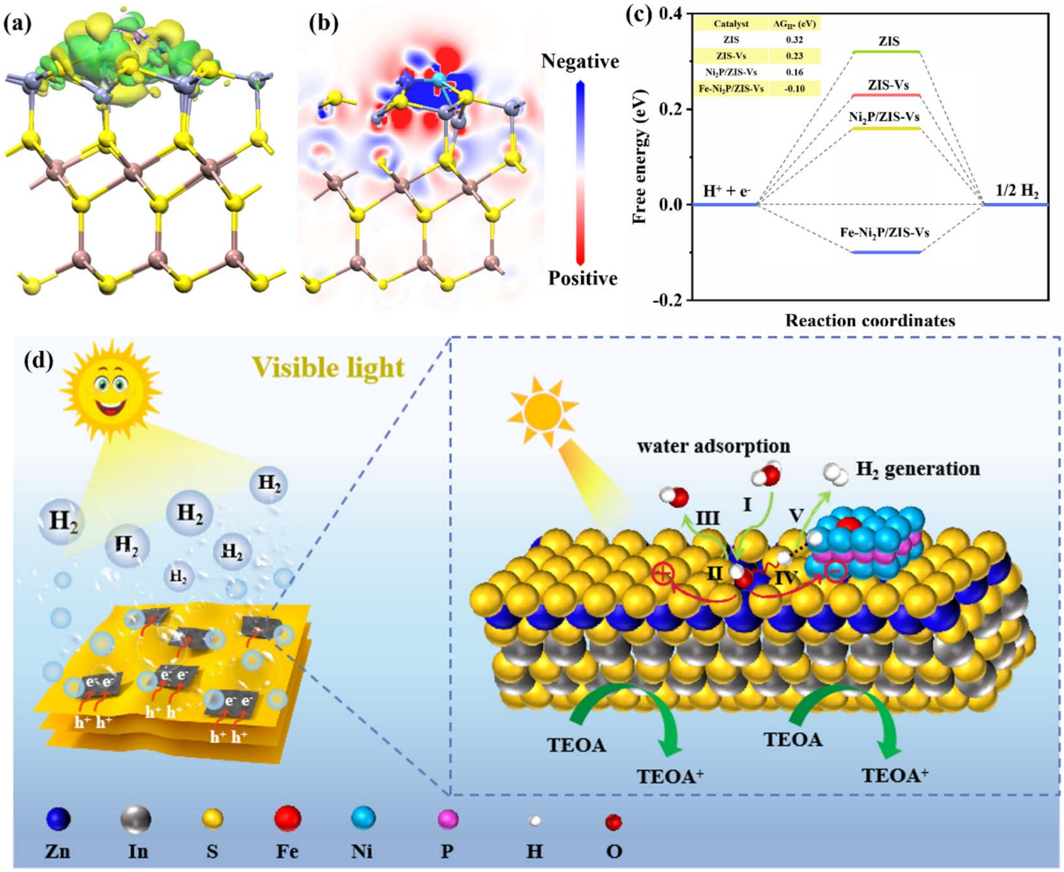

Fig. 5 (a) Charge density difference of the 3D-optimized structure model and (b) the corresponding longitudinal section image. (c) Hydrogen adsorption Gibbs free energy of ZIS, ZIS-Vs, Ni_2P/ZIS-Vs and Fe-Ni_2P/ZIS-Vs. (d) Proposed mechanism for photocatalytic H_2 evolution in the Fe-Ni_2P/ZIS-Vs system under visible-light irradiation.

compared with other materials, illustrating the optimal H adsorption/desorption ability of hydrogen evolution on Fe-Ni_2P/ZIS-Vs. First, loading Ni_2P on ZIS-Vs could build an internal electric field to effectively enhance charge separation and reduce the ΔG_{H^*}, thus promoting HER. Then, to further enhance the H* absorption at the hydrogen precipitation site Ni_2P, Fe dopant is introduced to adjust the adsorption/desorption of H*. Compared with Ni, Fe has a weak ability to provide electrons, so the doped Ni sites obtain fewer electrons, which improves the H* adsorption ability of the Ni sites and is conducive to HER. The above research demonstrated that S vacancy, cocatalyst Ni_2P and Fe doping could effectively promote carrier transfer, move down the center of the d-band, accelerate the dissociation of water molecules, reduce the adsorption energy of hydrogen evolution intermediates and fundamentally improve the HER of the catalyst.[58]

Combining the above experimental data and DFT calculations, a schematic diagram is given in Fig. 5d to explain the possible photocatalytic mechanism from the perspective of structure, charge transfer and transport pathways. As a typical n-type semiconductor, ZIS with an upward bending of the surface energy band and a positive voltage response, photogenerated carriers are easily bound together. Therefore, it has very low hydrogen evolution efficiency. Considering this, the introduction of S vacancies on the Zn surface as electron traps could enrich the photogenerated electron (e^-), therefore preventing its recombination with holes (h^+). In addition, Fe-Ni_2P is selectively grown on the Vs region of the ZIS to form a compact 2D–2D structure. Then, the photoexcited e^- transfers to Fe-Ni_2P rapidly through the tight interface, thus achieving the effective separation of photoinduced charge carriers. Moreover, XPS displacement analysis and DFT calculation confirm that photoexcited e^- could be easily transferred from ZIS-Vs to Fe-Ni_2P. Owing to the different charge distribution, H_2O molecules obtain e^- from the surface of ZIS-Vs, and then the e^- is filled in the π^* 4a orbital of H_2O, where the H–O bond is elongated. Therefore, H_2O molecules are decomposed, and new O–H bonds are formed on the surface of ZIS-Vs. Then, the hydroxyl group acquires e^- and converts them into active H* species, which are more inclined to adsorb on the Ni edge of the hydrogen evolution site Ni_2P.[59] Therefore, H* species release H_2 at Ni_2P site. From the perspective of architecture, because both phases are ultra-thin nanosheet structures, the composite photocatalyst constructed really has a larger contact area, shorter transmission distance and lower impedance, leading to increased reaction sites, improved carrier separation and migration efficiency, lower hydrogen evolution barrier and faster reaction kinetics, thus significantly enhancing the photocatalytic hydrogen evolution.

3. Conclusions

Overall, the 2D/2D Fe-Ni_2P/ZIS-Vs photocatalyst was successfully synthesized by solvothermal self-assembly and exhibited highly catalytic performance for hydrogen evolution under visible light. Through a series of characterization methods, performance tests and theoretical calculations, the relationship of formation-structure–property of photocatalysts is explored. For Fe-Ni_2P/ZIS-Vs, the S vacancy increases the electron trap well and selectively grows the hydrogen evolution site Ni_2P. Moreover, Fe doping modulates the d-band center of Ni_2P, which further reduces the reaction energy barrier of photocatalytic hydrogen production and facilitates the adsorption and activation of H_2O. Consequently, Fe-Ni_2P/ZIS-Vs photocatalyst exhibits an excellent hydrogen evolution activity of 4548.75 $\mu mol\ g^{-1}\ h^{-1}$, which is 11.51 fold greater than that of normal ZIS powder. This study announces the influence of surface engineering on photocatalytic activity, which also provides guidance for the design of efficient hydrogen evolution photocatalysts.

Conflicts of interest

There are no conflicts to declare.

Acknowledgements

This work is supported by the link project of the National Natural Science Foundation of China (51772158 and 21965025).

Notes and references

1 T. Takata, J. Z. Jiang, Y. Sakata, M. Nakabayashi, N. Shibata, V. Nandal, K. Seki, T. Hisatomi and K. Domen, *Nature*, 2020, **581**, 411–414.
2 R. T. Chen, Z. F. Ren, Y. Liang, G. H. Zhang, T. Dittrich, R. Z. Liu, Y. Liu, Y. Zhao, S. Pang, H. Y. An, C. W. Ni, P. W. Zhou, K. L. Han, F. T. Fan and C. Li, *Nature*, 2022, **610**, 296–301.
3 T. Hisatomi and K. Domen, *Nat. Catal.*, 2019, **2**, 387–399.
4 L. X. Zheng, F. Teng, X. Y. Ye, H. J. Zheng and X. S. Fang, *Adv. Energy Mater.*, 2020, **10**, 1902355.
5 Z. Wang, C. Li and K. Domen, *Chem. Soc. Rev.*, 2019, **48**, 2109–2125.
6 D. Voiry, H. S. Shin, K. P. Loh and M. Chhowalla, *Nat. Rev. Chem.*, 2018, **2**, 17105.
7 S. B. Wang, Y. Wang, S. L. Zhang, S. Q. Zang and X. W. D. Lou, *Adv. Mater.*, 2019, **31**, 1903404.
8 X. H. Wang, X. H. Wang, J. F. Huang, S. X. Li, A. Meng and Z. J. Li, *Nat. Commun.*, 2021, **12**, 4112.
9 S. B. Wang, B. Y. Guan and X. W. D. Lou, *J. Am. Chem. Soc.*, 2018, **140**, 5037–5040.
10 S. Cao, J. G. Yu, S. Wageh, A. A. Al-Ghamdi, M. Mousavi, J. B. Ghasemi and F. Y. Xu, *J. Mater. Chem. A*, 2022, **10**, 17174–17184.
11 Y. G. Chao, P. Zhou, J. P. Lai, W. Y. Zhang, H. W. Yang, S. Y. Lu, H. Chen, K. Yin, M. G. Li, L. U. Tao, C. S. Shang, M. P. Tong and S. J. Guo, *Adv. Funct. Mater.*, 2021, **31**, 2100923.
12 M. C. Liu, Y. B. Chen, J. Z. Su, J. W. Shi, X. X. Wang and L. J. Guo, *Nat. Energy*, 2016, **1**, 16151.
13 J. Lee, H. Kim, T. Lee, W. Jang, K. H. Lee and A. Soon, *Chem. Mater.*, 2019, **31**, 9148–9155.
14 G. Yadav and M. Ahmaruzzaman, *Inorg. Chem. Commun.*, 2022, **138**, 109288.
15 X. C. Jiao, Z. W. Chen, X. D. Li, Y. F. Sun, S. Gao, W. S. Yan, C. M. Wang, Q. Zhang, Y. Lin, Y. Luo and Y. Xie, *J. Am. Chem. Soc.*, 2017, **139**, 7586–7594.
16 J. H. Zheng, M. Y. Qi, Z. R. Tang and Y. J. Xu, *J. Mater. Chem. A*, 2023, **11**, 4013–4019.
17 J. Zhang, X. C. Liang, C. Zhang, L. H. Lin, W. D. Xing, Z. Y. Yu, G. G. Zhang and X. C. Wang, *Angew. Chem., Int. Ed.*, 2022, **61**, 202210849.
18 T. M. Su, C. Z. Men, L. Y. Chen, B. X. Chu, X. Luo, H. B. Ji, J. H. Chen and Z. Z. Qin, *Adv. Sci.*, 2022, **9**, 2103715.
19 Y. Z. Wang, D. Chen, L. S. Qin, J. H. Liang and Y. X. Huang, *Nat. Commun.*, 2021, **12**, 4112.
20 S. Q. Zhang, X. Liu, C. B. Liu, S. L. Luo, L. L. Wang, T. Cai, Y. X. Zeng, J. L. Yuan, W. Y. Dong, Y. Pei and Y. T. Liu, *ACS Nano*, 2018, **12**, 751–758.
21 F. Gao, R. Lei, X. Y. Huang, J. Yuan, C. K. Jiang, W. H. Feng, L. L. Zhang and P. Liu, *Appl. Catal., B*, 2021, **292**, 120187.
22 D. S. Dai, L. Wang, N. Xiao, S. S. Li, H. Xu, S. Liu, B. R. Xu, D. Lv, Y. Q. Gao, W. Y. Song, L. Ge and J. Liu, *Appl. Catal., B*, 2018, **233**, 194–201.
23 Z. C. Sun, M. S. Zhu, X. S. Lv, Y. Y. Liu, C. Shi, Y. Daid, A. J. Wang and T. Majima, *Appl. Catal., B*, 2019, **246**, 330–336.
24 Z. J. Sun, Q. D. Yue, J. S. Li, J. Xu, H. F. Zheng and P. W. Du, *J. Mater. Chem. A*, 2015, **3**, 10243–10247.
25 A. Indra, A. Acharjya, P. W. Menezes, C. Merschjann, D. Hollmann, M. Schwarze, M. Aktas, A. Friedrich, S. Lochbrunner, A. Thomas and M. Driess, *Angew. Chem., Int. Ed.*, 2017, **56**, 1653–1657.
26 I. Mondal, H. Lee, H. Kim and J. Y. Park, *Adv. Funct. Mater.*, 2020, **30**, 1908239.
27 X. D. Jing, N. Lu, J. D. Huang, P. Zhang and Z. Y. Zhang, *J. Energy Chem.*, 2021, **58**, 397–407.
28 R. J. Gao, L. Pan, H. W. Wang, X. W. Zhang, L. Wang and J. J. Zou, *ACS Catal.*, 2018, **8**, 8420–8429.
29 G. H. Zhang, X. X. Yuan, B. Xie, Y. Meng, Z. M. Ni and S. J. Xia, *Chem. Eng. J.*, 2022, **433**, 133670.
30 X. L. Li, X. J. Wang, J. Y. Zhu, Y. P. Li, J. Zhao and F. T. Li, *Chem. Eng. J.*, 2018, **353**, 15–24.
31 L. Zhang, J. H. Qiu, D. L. Dai, Y. C. Zhou, X. Liu and J. F. Yao, *J. Clean Prod.*, 2022, **341**, 130891.
32 F. S. Xing, C. C. Cheng, J. W. Zhang, Q. W. Liu, C. Chen and C. J. Huang, *Appl. Catal., B*, 2021, **285**, 119818.

33 S. Q. Zhang, Z. F. Zhang, Y. M. Si, B. Li, F. Deng, L. X. Yang, X. Liu, W. L. Dai and S. L. Luo, *ACS Nano*, 2021, **15**, 15238–15248.

34 S. M. Zhu, X. J. Qian, D. P. Lan, Z. Y. Yu, X. X. Wang and W. Y. Su, *Appl. Catal., B*, 2020, **269**, 118806.

35 Y. Hadeethi, E. Mkawi, O. Hartomy and E. Bekyarova, *Ceram. Int.*, 2021, **47**, 11568–11573.

36 B. Zhu, J. Zhou, L. Ni and G. Diao, *J. Solid State Chem.*, 2022, **305**, 122703.

37 Y. J. Wu, Y. Zhang, Y. R. Sui, Z. W. Wang, S. Q. Lv, M. B. Wei, Y. F. Sun, B. Yao, X. Y. Liu and L. L. Yang, *Ceram. Int.*, 2018, **44**, 11568–11573.

38 Y. N. Xue, P. H. Shao, M. L. Lin, Y. X. Yuan, W. X. Shi and F. Y. Cui, *J. Hazard. Mater.*, 2022, **428**, 128215.

39 J. H. Li, M. S. Han, Y. Guo, F. Wang and C. Sun, *Chem. Eng. J.*, 2016, **298**, 300–308.

40 Y. Wang, S. L. Wang, Y. B. Wu, Z. N. Wang, H. H. Zhang, Z. S. Cao, J. He, W. Li, Z. C. Yang, L. C. Zheng, D. Q. Feng, P. Pan, J. L. Bi, H. Y. Li, J. S. Zhao and K. L. Zhang, *J. Alloy Compd.*, 2021, **851**, 156733.

41 Z. Q. Wang, Z. L. Qi, X. J. Fan, D. Y. C. Leung, J. L. Long, Z. Z. Zhang, T. F. Miao, S. G. Meng, S. F. Chen and X. L. Fu, *Appl. Catal., B*, 2021, **281**, 119443.

42 C. C. Liu, T. Gong, J. Zhang, X. R. Zheng, J. Mao, H. Liu, Y. Li and Q. Y. Hao, *Appl. Catal., B*, 2020, **269**, 118806.

43 W. Z. Yuan, T. F. Jiang, X. Q. Fang, Y. Fan, S. Qian, Y. Y. Gao, N. Y. Cheng, H. G. Xue and J. Q. Tian, *Chem. Eng. J.*, 2022, **439**, 135743.

44 W. L. Zhen, X. F. Ning, B. J. Yang, Y. Q. Wu, Z. Li and G. X. Lu, *Appl. Catal., B*, 2018, **221**, 243–257.

45 J. Y. Wang, J. H. Wang, R. Shi, C. Zhou and T. R. Zhan, *Small Struct.*, 2023, **4**, 2200105.

46 L. L. Li, D. K. Ma, Q. L. Xu and S. M. Huang, *Chem. Eng. J.*, 2022, **437**, 135153.

47 H. T. Fan, Y. J. Jin, K. C. Liu and W. S. Liu, *Adv. Sci.*, 2022, **9**, 2104579.

48 X. Du, T. Y. Zhao, Z. Y. Xiu, Z. P. Xing, Z. Z. Li, K. Pan, S. L. Yang and W. Zhou, *Appl. Mater. Today*, 2020, **20**, 100719.

49 L. X. Meng, X. L. Zhou, S. Y. Wang, Y. Zhou, W. Tian, P. Kidkhunthod, S. Tunmee, Y. B. Tang, R. Long and Y. Xin, *Angew. Chem., Int. Ed.*, 2019, **58**, 16668–16675.

50 Y. C. Chen, Y. S. Huang, H. Huang, P. J. Su, T. P. Perng and L. J. Chen, *Nano Energy*, 2020, **67**, 104225.

51 Y. Wu, S. K. Yao, G. Z. Lv, Y. W. Wang, H. J. Zhang, P. L. Liao and Y. Wang, *J. Catal.*, 2021, **401**, 262–270.

52 L. Wei, D. Q. Zeng, J. Q. Liu, H. F. Zheng, T. Fujita, M. Y. Liao, C. Y. Li and Y. Z. Wei, *J. Colloid Interf. Sci.*, 2022, **608**, 3087–3097.

53 C. Q. Li, X. Du, S. Jiang, Y. Liu, Z. L. Niu, Z. Y. Liu, S. S. Yi and X. Z. Yue, *Adv. Sci.*, 2022, **9**, 2201773.

54 Y. K. Zhu, J. Ren, X. F. Yang, G. J. Chang, Y. Y. Bu, G. D. Wei, W. Han and D. J. Yang, *J. Mater. Chem. A*, 2017, **5**, 9952–9959.

55 Y. Lin, Q. Zhang, Y. H. Li, Y. P. Liu, K. J. Xu, J. N. Huang, X. S. Zhou and F. Peng, *ACS Sustain. Chem. Eng.*, 2020, **8**, 4537–4546.

56 C. Q. Li, X. Du, S. Jiang, Y. Liu, Z. L. Niu, Z. Y. Liu, S. S. Yi and X. Z. Yue, *Adv. Sci.*, 2022, **9**, 2201773.

57 X. H. Wang, X. H. Wang, J. F. Huang, S. X. Li, A. Meng and Z. J. Li, *Nat. Commun.*, 2021, **12**, 4112.

58 B. C. Qiu, P. Huang, C. Lian, Y. X. Ma, M. Y. Xing, H. L. Liu and J. L. Zhang, *Appl. Catal., B*, 2021, **298**, 120518.

59 Y. H. Peng, X. L. Guo, S. F. Xu, Y. N. Guo, D. S. Zhang, M. J. Wang, G. S. Wei, X. L. Yang, Z. Li, Y. Zhang and F. H. Tian, *J. Energy Chem.*, 2022, **75**, 276–284.